

Linking Dispersion and Stirring in Randomly Braiding Flows

Daniel R. Lester*

School of Engineering, RMIT University, Melbourne, Australia

Michael G. Trefry

Independent Researcher, Perth, Australia

Guy Metcalfe

Swinburne University of Technology, Melbourne, Australia

(Dated: December 10, 2024)

Many random flows, including 2D unsteady and stagnation-free 3D steady flows, exhibit non-trivial braiding of pathlines as they evolve in time or space. We show that these random flows belong to a pathline braiding *universality class* that quantitatively links dispersion and chaotic stirring, meaning that the Lyapunov exponent can be estimated from the purely advective transverse dispersivity. We verify this quantitative link for both unsteady 2D and steady 3D random flows. This result uncovers a deep connection between transport and mixing over a broad class of random flows.

Most steady and unsteady flows exhibit complex Lagrangian kinematics, whereby pathlines intertwine in a chaotic manner in space and time [1, 2]. Such Lagrangian chaos or chaotic advection [3, 4] arises from stretching and folding of fluid elements, leading to highly striated material distributions that profoundly augment many fluid-borne phenomena [5–7], including solute transport [8, 9], mixing [10, 11], chemical reactions [12, 13], biological activity [14, 15], particle transport [16, 17] and heat transfer [18, 19]. Complex stirring arises because the kinematic equation $\dot{\mathbf{x}}(t) = \mathbf{v}(\mathbf{x}, t)$ is rich enough to admit chaotic dynamics if the velocity field $\mathbf{v}(\mathbf{x}, t)$ possesses sufficient spatio-temporal degrees of freedom (dof ≥ 3) [20] and constraints such as symmetries in Stokes flow [21] or helicity in Darcy flow [22] are not imposed.

Unsteady 2D flows and stagnation-free steady 3D flows may be topologically unified by considering the former as the latter with unit velocity in time [23]. For these dof = 3 flows, the intertwining of pathlines may be formalised as a non-trivial *braiding* process [24], and a mathematical framework [25] and associated tools [26, 27] have been developed to quantify the topological complexity of the braiding motions. As pathlines are invariant 1D objects in a 3D continuum, non-trivial pathline braiding stretches and folds the interstitial continuum fluid in a chaotic manner (Fig. 1a) [24]. As the topological complexity of the braiding motions approximates that of the fluid flow [28], there exist deep connections between braiding complexity and the rate of chaotic stirring [29].

In addition to stirring, pathline braiding in unbounded random flows is also strongly linked to advective transverse particle dispersion as random pathlines must typically cross one another (with respect to an arbitrary reference direction) to separate without bound. Although there exist particular flows that do not braid but can disperse (e.g. hyperbolic flows) and vice-versa (e.g. confined braiding flows), these specific cases arise in ei-

ther bounded or deterministic flows. For unbounded random flows, strong links have been observed between non-trivial braiding and particle dispersion in 2D turbulence [30] and ferrofluids [31], while many studies [32] have uncovered links between particle dispersion and chaotic stirring. Conversely, steady 3D flows with zero helicity density [33, 34] $\mathcal{H}(\mathbf{x}) \equiv \mathbf{v}(\mathbf{x}) \cdot \nabla \times \mathbf{v}(\mathbf{x})$ are integrable [1] (non-chaotic) and admit a pair of streamfunctions $\psi_1(\mathbf{x})$, $\psi_2(\mathbf{x})$ [35, 36] that act as Euler potentials as $\mathbf{v}(\mathbf{x}) = \nabla\psi_1(\mathbf{x}) \times \nabla\psi_2(\mathbf{x})$. These potentials prohibit pathline braiding as streamlines are confined to level sets of $\psi_1(\mathbf{x})$, $\psi_2(\mathbf{x})$ and have been proved [37] to also prevent transverse particle dispersion. While these observations illustrate the strong correlations between chaotic stirring and particle dispersion in randomly braiding flows, lacking is a mechanistic understanding of the underlying link between these phenomena.

We examine the link between particle dispersion and braiding via simple random braiding models and show that there exists a pathline braiding *universality class* to which all 3 dof unbounded random flows belong. This reveals the deep connection between dispersion and chaotic stirring in randomly braiding 3 dof flows; moreover, this uncovers a quantitative link between the Lyapunov exponent λ_∞ and advective transverse dispersivity D_T . We validate the link for two example flows: an unsteady random 2D flow and an steady 3D random flow. The latter case is related to a proof of the ubiquity of chaotic advection in heterogeneous Darcy flow [38].

To elucidate the link between pathline braiding, chaotic advection and transverse dispersion, we begin with a particularly simple streamline model that, nonetheless, captures the essential features of a mean longitudinal steady chaotic 3D flow: namely braiding of streamlines as they propagate longitudinally in the x_1 direction. The unsteady 2D analog is a 2D flow with pathlines that braid in time t rather than x_1 . As shown

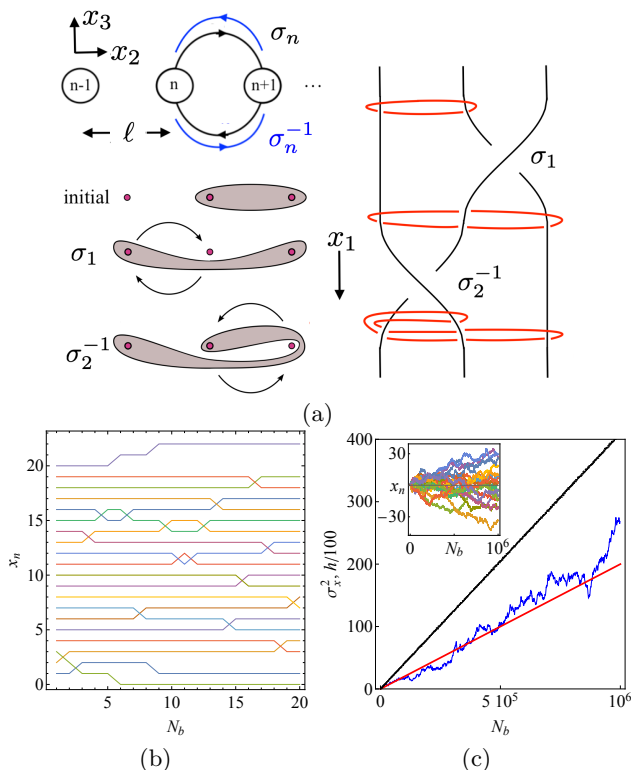


FIG. 1. (a) Top left: Schematic of the 1D streamline model including streamlines $n - 1$, n , $n + 1$ in the transverse $x_2 - x_3$ plane and clockwise (black) σ_n , anti-clockwise (blue) σ_n^{-1} braid generators. Bottom left: stretching of material elements due to braiding motions (adapted from [39]) that evolve with the longitudinal x_1 direction. Bottom right: braid diagram depicting stretching of material elements (red) around streamlines (black). (b) Braid diagram for $N_p = 20$ streamlines over $N_b = 20$ braiding actions in the x_1 direction, leading to non-trivial braiding and transverse dispersion. (c) Growth of topological entropy h (black line) and transverse variance $\sigma_{x_2}^2$ (blue line) with N_b , in agreement with (1) (red line). Inset: Brownian motion of streamlines with increasing N_b .

in Fig. 1a (top left), the 1D streamline model consists of a 1D array of N_p streamlines in \mathbb{R}^3 which propagate with uniform velocity in the x_1 direction and repeat periodically with uniform spacing $\Delta x_2 = \ell$ in the x_2 direction, where ℓ is the velocity correlation length.

At integer multiples of longitudinal distance $x_1 = \Delta_L$, one pair of neighbouring streamlines randomly exchange position via the clockwise or counter-clockwise rotations shown in Fig. 1a, which respectively are labelled by the *braid generators* σ_n and σ_n^{-1} for the streamline pair $(n, n + 1)$, with $n \in 1 : N_p - 1$. The sequence of N_b braid generators forms the braid word $\mathbf{b} = \sigma_{n_1}^{\pm 1} \sigma_{n_2}^{\pm 1} \dots \sigma_{n_{N_b}}^{\pm 1}$ that completely defines the braiding of streamlines. Due to periodicity the set of N_p streamlines undertake unbounded random walks along the x_2 coordinate as they propagate longitudinally. Fig. 1b shows the braid diagram for $N_p = 20$ streamlines undertaking $N_b = 20$

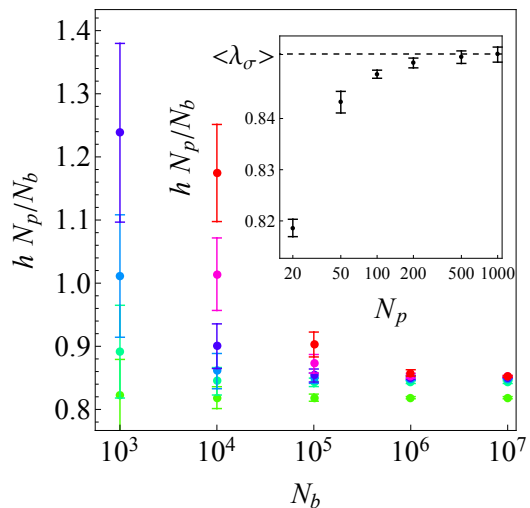


FIG. 2. Convergence of scaled mean topological entropy $N_p/N_b \langle h \rangle$ with braid number N_b for different streamline numbers N_p (green 50, light blue 100, purple 200, pink 500, red 1000). Dots indicate mean value, error bars indicate \pm standard error. Inset: convergence of scaled mean topological entropy $h N_p/N_b$ for $N_b = 10^7$ with streamline number N_p to random braid entropy $\langle \lambda_\sigma \rangle$.

random braid actions, illustrating braiding actions and transverse dispersion of streamlines.

Fig. 1a shows that streamline braiding can lead to rapid stretching of material elements. If the braiding is non-trivial (pseudo-Anosov) [24], this stretching grows exponentially with the number N_b of braiding actions, the growth rate of which is quantified by the topological braid entropy h [39] which converges to the topological entropy \hat{h} of the underlying fluid flow in the limit of large N_p [28]. Hence for statistically stationary random flows, the braid entropy h converges to the Lyapunov exponent $\hat{\lambda}_\infty$ of the associated chaotic flow in the limit of large N_p and N_b [29]. To construct a random braiding sequence we chose N_b braid generators with equal probability from the set $\{\sigma_1, \sigma_1^{-1}, \dots, \sigma_{N_p}, \sigma_{N_p}^{-1}\}$, and calculate the topological entropy h via the *braidlab* package [40]. Streamline braiding in this model is governed by the correlation length ℓ , and in [41] we show that additional streamlines (i.e. $\Delta x_2 < \ell$) only contribute trivial braiding motions and so do not alter the braiding entropy h .

Fig. 1c shows the topological entropy h grows linearly with N_b , indicating such random braiding generates exponential growth of material elements. As two of the N_p streamlines make random jumps in the x_2 direction of $\pm \ell$ with each braiding event, the spatial variance $\sigma_{x_2}^2$ of streamlines grows linearly with N_b as

$$\sigma_{x_2}^2(t) = \sigma_{x_2,0}^2(0) + 2\ell^2 \frac{N_b}{N_p} \equiv \sigma_{x_2,0}^2(0) + 2D_T t, \quad (1)$$

where $N_b = \langle v_1 \rangle t / \Delta_L$, D_T is the transverse dispersivity and $\langle v_1 \rangle$ is the mean longitudinal velocity. As shown in

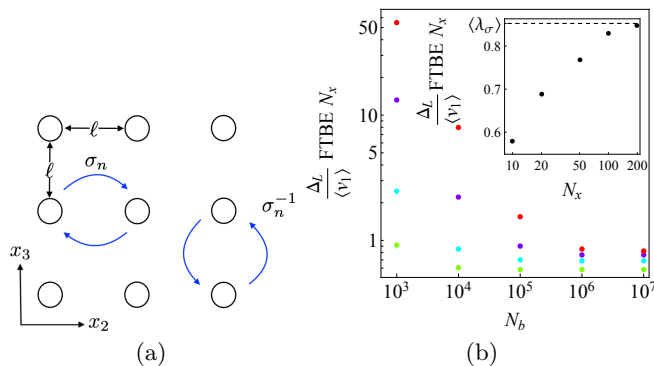


FIG. 3. (a) Schematic of 2D streamline model. (b) Convergence of scaled FTBE with N_b for the 2D streamline model for different N_x (green $N_x = 10$, light blue $N_x = 20$, purple $N_x = 50$, pink $N_x = 100$, red $N_x = 200$). Inset: convergence of scaled FTBE for $N_b = 10^7$ with N_x to $\langle \lambda_\sigma \rangle$.

Fig. 1c, this predicted Brownian motion agrees well with model observations.

Fig. 2 shows that for 10^3 realisations of random braids with N_p particles and N_b braids, $N_b/N_p \langle h \rangle$ converges to the *random braid entropy* $\langle \lambda_\sigma \rangle$

$$\lim_{N_p, N_b \rightarrow \infty} \frac{N_p}{N_b} \langle h \rangle \rightarrow \langle \lambda_\sigma \rangle \approx 0.8529 \approx \frac{2}{3} \left(\frac{2\pi}{3} \right)^{1/3}, \quad (2)$$

which quantifies the topological braiding entropy of unbounded random 3 dof flows. Hence for this model the dimensionless Lyapunov exponent $\lambda_\infty \equiv \hat{\lambda}_\infty \ell / \langle v_1 \rangle$ is linearly related to the transverse dispersivity D_T as

$$\lambda_\infty = \frac{\langle \lambda_\sigma \rangle}{Pe_T}. \quad (3)$$

where $Pe_T \equiv D_T / (\langle v_1 \rangle \ell)$ is the advective transverse Péclet number. This linear relationship is expected as the 1D streamline model generates transverse dispersion and chaotic advection in equal measure.

To extend this model to 2D, we consider a periodic square array of $N_p = N_x \times N_x$ streamlines in the $x_2 - x_3$ plane with spacing $\Delta x_2 = \Delta x_3 = \ell$ as shown in Fig. 8a. Similar to the 1D model, rotations of pairs of adjacent streamlines are chosen at random, but streamline pairs may now be chosen in either direction, leading to linear variance growth

$$\sigma_{x_2}^2(t) = \sigma_{x_3}^2(t) = \sigma_0^2 + \frac{2}{d} \ell^2 \frac{N_b}{N_p} = \sigma_0^2 + 2D_T t, \quad (4)$$

where the factor of $2/d$ (where d is the dimension of the streamline array) arises as each rotation moves two streamlines by $\pm \ell$ in the x_2/x_3 direction $1/d$ of the time.

For the 2D streamline model, determination of the braid word from the sequence of braiding events is more complex. Hence the braiding topological complexity is quantified [41] in *braidlabb* via the finite time braiding

exponent (FTBE), an analogue of the finite time Lyapunov exponent which converges to h as $\lim_{t \rightarrow \infty} h/t \rightarrow \lim_{t \rightarrow \infty} \text{FTBE} = \hat{\lambda}_\infty$ [39, 42]. In [41] we establish convergence of the scaled FTBE and scaled h to $\langle \lambda_\sigma \rangle$ with increasing N_b for the 1D streamline model over 10^3 realisations. As the FTBE is normalised by the advection time t over which the braiding occurs, the FTBE has units of inverse time and so the prefactor $\Delta_L / \langle v_1 \rangle$ renders the scaled FTBE dimensionless.

For each braid word, the corresponding streamlines are constructed (see Fig. 8b) that resolve the clockwise and anti-clockwise rotations, and the *databraid* routine is used to compute the FTBE from these streamlines. The topological entropy is also computed in the usual manner via the *annbraid* routine in *braidlabb*. In the limit of large particle numbers N_p and braid events N_b , the scaled FTBE and topological entropy converge to each other and the random braiding exponent $\langle \lambda_\sigma \rangle$.

For the 2D model, we construct 3D streamline trajectories (shown in [41]) from a random braiding sequence and compute the FTBE. Fig. 8b shows convergence of the scaled average FTBE over 10 realisations to the random braid entropy with increasing N_b , N_p as $\lim_{N_b \rightarrow \infty} \lim_{N_p \rightarrow \infty} \frac{\Delta_L}{\langle v_1 \rangle} \text{FTBE } N_x \rightarrow \langle \lambda_\sigma \rangle$. Budišić and Thiffeault [42] show that in limit of long times and large particle numbers the FTBE converges to the Lyapunov exponent $\hat{\lambda}_\infty$, hence

$$\frac{\ell}{\langle v_1 \rangle} \lim_{N_b \rightarrow \infty} \lim_{N_p \rightarrow \infty} \text{FTBE} = \lambda_\infty, \quad (5)$$

and so the Lyapunov exponent is related to $\langle \lambda_\sigma \rangle$ as

$$\lambda_\infty = \frac{\ell}{\langle v_1 \rangle} \text{FTBE} = \langle \lambda_\sigma \rangle \frac{\ell}{\Delta_L} \frac{1}{N_x}. \quad (6)$$

and using (4) yields an expression consistent with (3)

$$\lambda_\infty^d = \langle \lambda_\sigma \rangle^d \left(\frac{\ell}{\Delta_L} \right)^{d-1} \frac{d}{Pe_T}, \quad d = 1, 2. \quad (7)$$

In [41], we extend the 2D streamline model to a 2D random walk model (Fig. 10a) which, following [39], is comprised of N_p random streamlines in the domain $\Omega : (x_1, x_2, x_3) \in [0, \infty) \times [0, L] \times [0, L]$ that make random jumps of magnitude Δ_T in the $x_2 - x_3$ plane at integer multiples of the longitudinal distance $x_1 = \Delta_L$. As shown in Fig. 10b, the scaled FTBE for this system also converges to $\langle \lambda_\sigma \rangle$ for different jump sizes Δ_T , and recovers [41] the relationship (7) between transverse dispersivity and Lyapunov exponent.

The persistence of (7) and $\langle \lambda_\sigma \rangle$ suggests that these diverse models all belong to the same *universality class* [43] associated with streamline braiding. This shows that chaotic advection and transverse dispersion are intimately linked in unbounded random 3 dof flows because they are both driven by non-trivial streamline braiding.

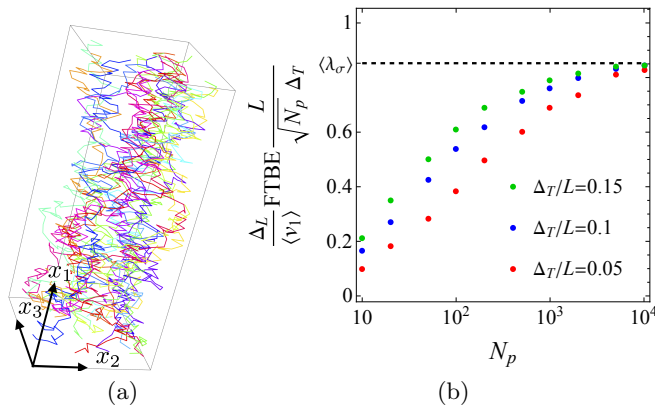


FIG. 4. (a) Schematic of 2D random walk streamline model. (b) Convergence of scaled FTBE to $\langle \lambda_\sigma \rangle$ for $N_b = 10^6$ with N_p for different values of Δ_T/L .

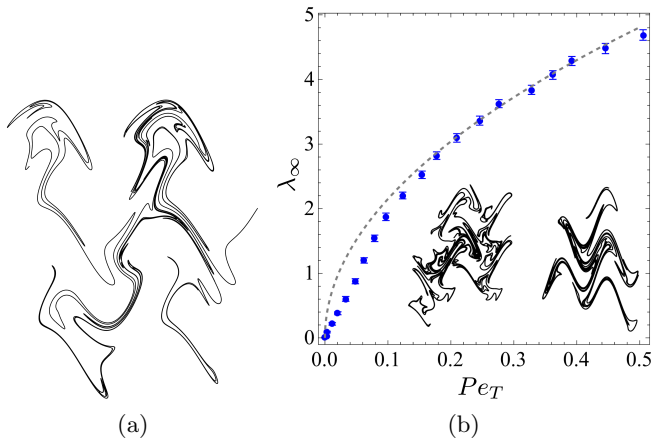


FIG. 5. (a) Dispersion, stretching and folding of a material line in a realisation of the TPRSf for $T = 0.5$. (b) Correlation between Lyapunov exponent λ_∞ and transverse Péclet number Pe_T from (7) (dashed line) and numerical simulations (blue dots). Insets show typical material lines for $T = 0.25$ (left) and $T = 0.5$ (right).

To examine the connection between dispersion, stirring and braiding in unsteady 2D flows, we consider the time-periodic random sine flow (TPRSF) [44]

$$\mathbf{v}(\mathbf{x}, t) = \begin{cases} (0, \sin(2\pi x_1 + \zeta)) & 0 \leq \text{mod}(t, T) < T/2, \\ (\sin(2\pi x_2 + \zeta), 0) & T/2 \leq \text{mod}(t, T) < T, \end{cases} \quad (8)$$

where the phase angle $\zeta \in [0, 2\pi]$ are random uniformly distributed variables and the flow period $T \in [0, 1]$ controls the transition from non-chaotic steady flow at $T = 0$ to chaotic dynamics for $T > 0$. Fig. 5a shows that under the non-trivial braiding action of the flow, tracer particles disperse outwards in the x_1 and x_2 directions, and material lines are stretched and folded in a complex manner. Fig. 5b shows the Lyapunov exponent λ_∞ calculated for 10^4 independent tracer particles (see [41] for details)

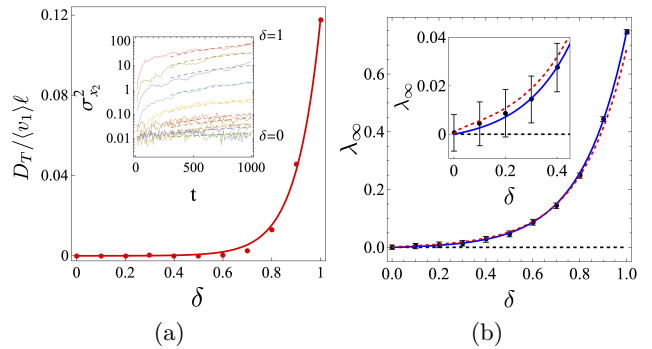


FIG. 6. (a) Growth of transverse Péclet number Pe_T with δ from simulations (red points), and fitted exponential function (red curve). Inset shows temporal evolution of transverse variance. (b) Growth of Lyapunov exponent λ_∞ with perturbation parameter δ from simulations (black points), and fitted exponential (blue curve). Error bars correspond to \pm two standard deviations $\sigma_{\epsilon_{22}^2}$. (red dotted curve) Lyapunov exponent predicted from fitted exponential in (b) and (7).

and the transverse Péclet number Pe_T calculated for 10^6 tracer particles (see [41] for details) for various values of $T \in [0, 1]$. The grey dashed line in Fig. 5b shows the predicted Lyapunov exponent from (7), which is in excellent agreement with the numerical data.

To examine this connection for steady 3D flow, we consider heterogeneous Darcy flow governed by

$$\mathbf{v}(\mathbf{x}) = -\mathbf{K}(\mathbf{x}) \cdot \nabla \phi(\mathbf{x}), \quad \nabla \cdot \mathbf{v} = 0, \quad (9)$$

in a triply-periodic unit cube (3-torus \mathbb{T}^3) $\mathcal{D} : \mathbf{x} \in [0, 1] \times [0, 1] \times [0, 1]$ driven by a unit potential gradient $\nabla \phi = \{-1, 0, 0\}$. We consider a heterogeneous porous medium with the following hydraulic conductivity field

$$\mathbf{K}(\mathbf{x}) = k_0(\mathbf{x})\mathbf{I} + \delta(k_\delta(\mathbf{x}) - k_0(\mathbf{x}))\hat{\mathbf{e}}_1 \otimes \hat{\mathbf{e}}_1, \quad (10)$$

where $k_0(\mathbf{x}) \neq k_\delta(\mathbf{x})$ and the perturbation parameter $\delta \in [0, 1]$ quantifies the deviation of the conductivity tensor from isotropy, and the scalar log-conductivity fields $f(\mathbf{x}) \equiv \ln k(\mathbf{x})$ are given by the random Fourier modes with correlation length $\ell = 1/4$ and log-variance $\sigma_{\ln K}^2 = 4$, as detailed in [41]. This is the simplest possible conductivity field that admits non-zero total helicity $H \equiv \int_{\mathcal{D}} d^3\mathbf{x} \mathcal{H}(\mathbf{x})$ [38]. Details regarding computation of the velocity field and streamlines, transverse dispersivity D_T and Lyapunov exponent λ_∞ are given in [41].

Fig. 6a shows that the transverse Péclet number Pe_T increases exponentially with δ as $Pe_T \approx 0.00381(e^{5.283\delta} - 1)$, indicating transverse dispersion arises for weak perturbations away from isotropic Darcy flow. Fig. 6b shows that the Lyapunov exponent λ_∞ also increases exponentially with δ as $\lambda_\infty \approx 4.343 \times 10^{-6}(e^{10.214\delta} - 1)$, and is also non-zero for small $\delta > 0$, indicating that chaotic advection occurs for weak perturbations away from heterogeneous isotropic Darcy flow.

Fig. 6b also shows that insertion of the fitted exponential for Pe_T into (7) (assuming $\Delta_L = \ell$ due to isotropy of the fields k_0, k_δ) yields excellent agreement with the measured Lyapunov exponent.

These results clearly demonstrate a fundamental relationship between dispersion and chaotic stirring across a diverse range of random 3 dof flows. The connection arises as both processes are generated by random pathline braiding. The existence of a pathline braiding universality class is demonstrated by the persistence of the universal braiding entropy $\langle \lambda_\sigma \rangle$ and the simple relationship (7) linking these phenomena over a wide range of random flows. This link is especially important for steady 3D heterogeneous Darcy flow, as it forms the basis of a proof [38] of the ubiquity of chaotic advection in these flows. More broadly, the existence of a quantitative link between advective dispersion and chaotic stirring in unbounded random 3 dof flows provides insights into their fundamental kinematics and has implications for understanding, quantifying and predicting transport and mixing in such flows.

We are pleased to acknowledge helpful discussions with J.-L. Thiffeault.

* daniel.lester@rmit.edu.au

- [1] V. I. Arnold, "Sur la topologie des écoulements stationnaires des fluides parfaits," *Comptes Rendus Acad. Sci. Paris* **261**, 312–314 (1965).
- [2] M. Hénon, "Sur la topologie des lignes de courant dans un cas particulier," *Comptes Rendus Acad. Sci. Paris* **262**, 312–314 (1966).
- [3] H. Aref, "Stirring by chaotic advection," *Journal of Fluid Mechanics* **143**, 1–21 (1984).
- [4] J. M. Ottino, *The Kinematics of Mixing: Stretching, Chaos, and Transport* (Cambridge University Press, Cambridge, United Kingdom, 1989).
- [5] Hassan Aref, John R Blake, Marko Budišić, Silvana SS Cardoso, Julyan HE Cartwright, Herman JH Clercx, Kamal El Omari, Ulrike Feudel, Ramin Golestanian, Emmanuelle Guillard, *et al.*, "Frontiers of chaotic advection," *Reviews of Modern Physics* **89**, 025007 (2017).
- [6] G. Metcalfe, M.F.M. Speetjens, D.R. Lester, and H.J.H. Clercx, "Beyond passive: Chaotic transport in stirred fluids," (Elsevier, 2012) pp. 109 – 188.
- [7] Michel Speetjens, Guy Metcalfe, and Murray Rudman, "Lagrangian Transport and Chaotic Advection in Three-Dimensional Laminar Flows," *Applied Mechanics Reviews* **73**, 030801 (2021).
- [8] S. W. Jones and W. R. Young, "Shear dispersion and anomalous diffusion by chaotic advection," *Journal of Fluid Mechanics* **280**, 149–172 (1994).
- [9] D. R. Lester, G. Metcalfe, and M. G. Trefry, "Anomalous transport and chaotic advection in homogeneous porous media," *Phys. Rev. E* **90**, 063012 (2014).
- [10] Stefano Cerbelli, Massimiliano Giona, Olexander Gorodetskyi, and Patrick D. Anderson, "Singular eigenvalue limit of advection-diffusion operators and properties of the strange eigenfunctions in globally chaotic flows," *The European Physical Journal Special Topics* **226**, 2247–2262 (2017).
- [11] D. R. Fereday and P. H. Haynes, "Scalar decay in two-dimensional chaotic advection and batchelor-regime turbulence," *Physics of Fluids* **16**, 4359–4370 (2004).
- [12] Tamás Tél, Alessandro de Moura, Celso Grebogi, and György Károlyi, "Chemical and biological activity in open flows: A dynamical system approach," *Physics Reports* **413**, 91 – 196 (2005).
- [13] Z. Neufeld and E. Hernandez-Garcia, *Chemical and biological processes in fluid flows: A dynamical systems approach* (Imperial College Press, 2009).
- [14] Tamás Tél, György Károlyi, Áron Péntek, István Scheuring, Zoltán Toroczkai, Celso Grebogi, and James Kadtke, "Chaotic advection, diffusion, and reactions in open flows," *Chaos: An Interdisciplinary Journal of Nonlinear Science* **10**, 89–98 (2000).
- [15] György Károlyi, Áron Péntek, István Scheuring, Tamás Tél, and Zoltán Toroczkai, "Chaotic flow: The physics of species coexistence," *Proceedings of the National Academy of Sciences* **97**, 13661–13665 (2000).
- [16] Nicholas T Ouellette, PJJ O'Malley, and Jerry P Gollub, "Transport of finite-sized particles in chaotic flow," *Phys. Rev. Lett.* **101**, 174504 (2008).
- [17] George Haller and Themistoklis Sapsis, "Where do inertial particles go in fluid flows?" *Physica D: Nonlinear Phenomena* **237**, 573 – 583 (2008).
- [18] D.R. Lester, M. Rudman, and G. Metcalfe, "Low reynolds number scalar transport enhancement in viscous and non-newtonian fluids," *International Journal of Heat and Mass Transfer* **52**, 655–664 (2009).
- [19] O. Baskan, M. F. M. Speetjens, G. Metcalfe, and H. J. H Clercx, "Direct experimental visualization of the global hamiltonian progression of two-dimensional lagrangian flow topologies from integrable to chaotic state," *Chaos: An Interdisciplinary Journal of Nonlinear Science* **25**, 103106 (2015).
- [20] H. Poincaré, *Théorie des tourbillons*, Réimpressions (Editions Jacques Gabay) (Jacques Gabay, 1893).
- [21] G Haller and I Mezic, "Reduction of three-dimensional, volume-preserving flows with symmetry," *Nonlinearity* **11**, 319 (1998).
- [22] Guy Metcalfe, Daniel Lester, and Michael Trefry, "A primer on the dynamical systems approach to transport in porous media," *Transport in Porous Media* **146**, 55–84 (2023).
- [23] K. Bajer, "Hamiltonian formulation of the equations of streamlines in three-dimensional steady flows," *Chaos, Solitons and Fractals* **4**, 895–911 (1994).
- [24] Philip L. Boyland, Hassan Aref, and Mark A. Stremler, "Topological fluid mechanics of stirring," *Journal of Fluid Mechanics* **403**, 277–304 (2000).
- [25] Michael Handel and William P Thurston, "New proofs of some results of nielsen," *Advances in Mathematics* **56**, 173–191 (1985).
- [26] Jacques-Olivier Moussafrir, "On computing the entropy of braids," *Functional Analysis and Other Mathematics* **1**, 37–46 (2006).
- [27] M. Bestvina and M. Handel, "Train-tracks for surface homeomorphisms," *Topology* **34**, 109–140 (1995).
- [28] Jean-Luc Thiffeault, "Braids of entangled particle trajectories," *Chaos: An Interdisciplinary Journal of Nonlinear Science* **15**, 103106 (2005).

- Science **20**, 017516 (2010).
- [29] Jean-Luc Thiffeault, “Measuring topological chaos,” Phys. Rev. Lett. **94**, 084502 (2005).
- [30] Nicolas Francois, Hua Xia, Horst Punzmann, Benjamin Faber, and Michael Shats, “Braid entropy of two-dimensional turbulence,” Scientific Reports **5**, 18564 (2015).
- [31] Arne T. Skjeltorp, Sigmund Clausen, and Geir Helgesen, “Application of braid statistics to particle dynamics,” Physica A: Statistical Mechanics and its Applications **274**, 267–280 (1999).
- [32] Thomas Sunn Pedersen, Poul K. Michelsen, and Jens Juul Rasmussen, “Lyapunov exponents and particle dispersion in drift wave turbulence,” Physics of Plasmas **3**, 2939–2950 (1996).
- [33] H. K. Moffatt, “The degree of knottedness of tangled vortex lines,” Journal of Fluid Mechanics **1**, 117–129 (1969).
- [34] Jean Jacques Moreau, “Constantes d’un îlot tourbillonnaire en fluide parfait barotrope,” Comptes Rendus Acad. Sci. Paris **252**, 2810–2812 (1961).
- [35] Z. Yoshida, “Clebsch parameterization: Basic properties and remarks on its applications,” Journal of Mathematical Physics **50**, 113101 (2009).
- [36] Daniel R. Lester, Marco Dentz, Aditya Bandopadhyay, and Tanguy Le Borgne, “The Lagrangian kinematics of three-dimensional Darcy flow,” Journal of Fluid Mechanics **918**, A27 (2021).
- [37] Daniel R. Lester, Marco Dentz, Prajwal Singh, and Aditya Bandopadhyay, “Under what conditions does transverse macrodispersion exist in groundwater flow?” Water Resources Research **59**, e2022WR033059 (2023).
- [38] Daniel R. Lester and Marco Dentz, “Equating topological entropy and lyapunov exponent in ergodic flows,” Physical Review Fluids (2024).
- [39] Jean-Luc Thiffeault, *Braids and Dynamics* (Springer Cham, 2022).
- [40] Jean-Luc Thiffeault and Marko Budišić, “Braidlab: A software package for braids and loops,” (2013–2021), 3.2.5.
- [41] “Supplementary material,”.
- [42] Marko Budišić and Jean-Luc Thiffeault, “Finite-time braiding exponents,” Chaos: An Interdisciplinary Journal of Nonlinear Science **25**, 087407 (2015).
- [43] Géza Ódor, “Universality classes in nonequilibrium lattice systems,” Rev. Mod. Phys. **76**, 663–724 (2004).
- [44] M. M. Alvarez, F. J. Muzzio, S. Cerbelli, A. Adrover, and M. Giona, “Self-similar spatiotemporal structure of intermaterial boundaries in chaotic flows,” Phys. Rev. Lett. **81**, 3395–3398 (1998).
- [45] Sanjiva K. Lele, “Compact finite difference schemes with spectral-like resolution,” Journal of Computational Physics **103**, 16–42 (1992).
- [46] Daniel R. Lester, Aditya Bandopadhyay, Marco Dentz, and Tanguy Le Borgne, “Hydrodynamic dispersion and lamb surfaces in darcy flow,” Transport in Porous Media **130**, 903–922 (2019).
- [47] Daniel R. Lester, Marco Dentz, Aditya Bandopadhyay, and Tanguy Le Borgne, “Fluid deformation in isotropic Darcy flow,” Journal of Fluid Mechanics **945**, A18 (2022).
- [48] D. R. Lester, M. Dentz, T. Le Borgne, and F. P. J. De Barros, “Fluid deformation in random steady three-dimensional flow,” Journal of Fluid Mechanics **855**, 770–803 (2018).
- [49] Tanguy Le Borgne, Marco Dentz, and Jesus Carrera, “Lagrangian statistical model for transport in highly heterogeneous velocity fields,” Phys. Rev. Lett. **101**, 090601 (2008).
- [50] Tanguy Le Borgne, Marco Dentz, and Jesus Carrera, “Spatial markov processes for modeling lagrangian particle dynamics in heterogeneous porous media,” Phys. Rev. E **78**, 026308 (2008).

Invariance of Topological Braiding Entropy with Streamline Density

To show that decreasing streamline spacing Δx_2 below $\Delta x_2 = \ell$ does not impact the braiding exponent in the 1D streamline model, we consider doubling the streamline resolution to $\Delta x_2 = \ell/2$, such that the number of streamlines increases from N_p to $2N_p - 1$ and the corresponding streamline numbers map as $i \mapsto 2i - 1$. This change then corresponds to having 3 neighbouring streamlines rotate together during a clockwise or anti-clockwise re-orientation event. Under this change, the clockwise and anticlockwise braid generators are then mapped from the $\Delta x_2 = \ell$ streamline model to the $\Delta x_2 = \ell/2$ model as

$$\sigma_i^{\pm 1} \mapsto \sigma_{2i-1}^{\pm 1} \sigma_{2i}^{\pm 1} \sigma_{2i-1}^{\pm 1}. \quad (11)$$

For example, the pigtail braid with $N_p = 3$ particles shown in Fig. 7a has braid word $\mathbf{b} = \sigma_1 \sigma_2^{-1}$, which results in topological entropy $h = \ln[(\sqrt{5} + 3)/2]$ [39]. Doubling of the spatial resolution of the streamlines to $N_p = 5$ particles via (11) results in the braid diagram shown in shown in Fig. 7b with corresponding braid word $\mathbf{b} = \sigma_1 \sigma_2 \sigma_1 \sigma_3^{-1} \sigma_4^{-1} \sigma_3^{-1}$, which has exactly the same topological entropy. This is because the additional streamlines do no contribute to the topological complexity of the braiding motions. As they are added on a lengthscale Δx_2 less than the correlation length ℓ , these additional streamlines do not resolve any hitherto hidden stirring actions, they simply move in accordance with the stirring motions resolved by the original set of streamlines. Similar invariance of the topological braiding entropy to streamline resolution resolution below $\Delta x_2 = \ell$ is obtained for numerical tests (not shown) of random braiding protocols subject to (11).

Extension of 1D Streamline Model to 2D

To extend the 1D streamline model introduced in the main body of the paper to 2D, we consider a square array of $N_p = N_x \times N_x$ streamlines in the $x_2 - x_3$ plane with spacing $\Delta x_2 = \Delta x_3 = \ell$ as shown in Fig. 8a. Similar to the 1D model, clockwise and anti-clockwise rotations of pairs of adjacent streamlines are chosen at random, but with the variation that adjacent streamlines may now be chosen in both the x_2 and x_3 directions. Under this 2D

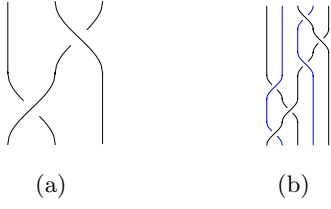


FIG. 7. (a) Braid diagram for pigtail braid involving $N_p = 3$ streamlines. (b) Braid diagram for pigtail braid involving $N_p = 5$ streamlines. Additional streamlines (blue) only undergo trivial braiding and so do not contribute to topological entropy h .

model the spatial variance in the x_2 and x_3 directions then evolve as

$$\sigma_{x_2}^2(t) = \sigma_{x_3}^2(t) = \sigma_0^2 + \frac{2}{d}\ell^2 \frac{N_b}{N_p} = \sigma_0^2 + \frac{2}{d}\ell^2 \frac{1}{N_p} \frac{\langle v_1 \rangle}{\Delta_L} t, \quad (12)$$

where $\Delta_L = x_1/N_b$ is the distance between braiding events in the x_1 direction. The factor of $2/d$ (where $d = 2$ is the Euclidean dimension of the streamline array) associated with the $\ell^2 N_b/N_p$ term arises as each braid event moves two of the N_p streamlines by $\pm\ell$ in the x_2 direction $1/d$ of the time and the x_3 direction in the other $1/d$. Similarly, the streamline variance due to transverse dispersivity D_T grows as

$$\sigma_{x_2}^2(t) = \sigma_{x_3}^2(t) = \sigma_0^2 + 2D_T t, \quad (13)$$

hence the transverse dispersivity is related to the model parameters as

$$D_T = \frac{\ell^2 \langle v_1 \rangle}{dN_p \Delta_L}. \quad (14)$$

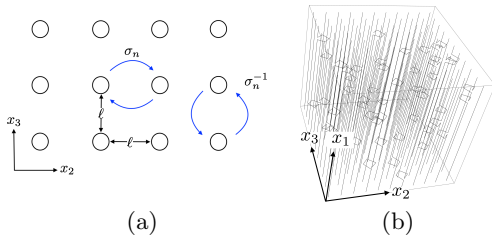


FIG. 8. (a) Schematic of streamline braiding in 2D streamline model. (b) Corresponding streamlines for $N_p = N_x \times N_x = 10 \times 10$ 2D array of streamlines. Helical streamline structures correspond to clockwise and counter-clockwise braiding motions depicted in (a).

For the 2D streamline model, determination of the sequence of braid generators (braid word) from the sequence of braiding events is more complex. This is because a single braid event involving the exchange of position of two streamlines involves the crossing of

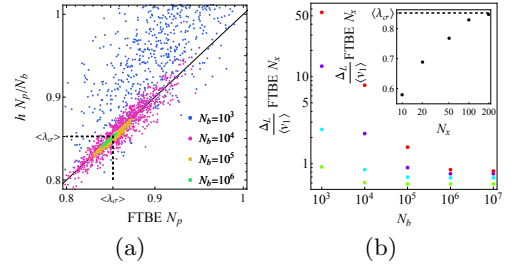


FIG. 9. (a) Convergence of scaled FTBE (N_p FTBE) and scaled topological entropy (hN_p/N_b) to the random braid entropy ($\langle \lambda_\sigma \rangle$) for the 1D streamline model with the number N_b of braid events for fixed streamline number $N_p = 10^3$. Similar results are obtained for larger values of N_p . (b) Convergence of scaled FTBE ($\Delta_L/\langle v_1 \rangle$ FTBE N_x) with braid number N_b for the 2D streamline model for different array dimensions N_x (green $N_x = 10$, light blue $N_x = 20$, purple $N_x = 50$, pink $N_x = 100$, red $N_x = 200$). Inset: convergence of scaled FTBE for $N_b = 10^7$ with streamline array dimension N_x to $\langle \lambda_\sigma \rangle \approx 0.8525$.

these streamlines over many of the other streamlines in the array (depending upon the projection angle used to characterise the crossings [29]). To circumvent this problem, for a given sequence of randomly chosen braid events we construct N_p streamline trajectories which resolve the clockwise and anti-clockwise motions of each braiding event. The resultant braid word is computed from the trajectory data using the *databraid* routine in *braidlab*. As the corresponding braid is not closed, the finite time braiding exponent (FTBE) [42], an analogue of the finite time Lyapunov exponent (FTLE), is used to quantify the degree of entanglement of streamlines. Budišić and Thiffeault [42] show that as the number of braiding events N_b grows, the FTBE converges to the topological entropy of the braid divided by the elapsed time over which N_b has occurred.

Fig. 9a shows convergence of the scaled FTBE ($\Delta_L/\langle v_1 \rangle$ FTBE N_p) to the scaled topological entropy (hN_p/N_b) with increasing number of braid events N_b for the 1D streamline model over 10^3 realisations of random braiding sequences. As the FTBE is normalised by the advection time t over which the braiding occurs, the FTBE has units of inverse time and so the prefactor $\Delta_L/\langle v_1 \rangle$ renders the scaled FTBE dimensionless. For each braid word, the corresponding streamlines are constructed (see Fig. 8b) that resolve the clockwise and anti-clockwise rotations, and the *databraid* routine is used to compute the FTBE from these streamlines. The topological entropy is also computed in the usual manner via the *annbraid* routine in *braidlab*. In the limit of large particle numbers N_p and braid events N_b , the scaled FTBE and topological entropy converge to each other and the random braiding exponent ($\langle \lambda_\sigma \rangle$).

For the 2D streamline model, we construct the streamline trajectories shown in Fig. 8b from the sequence of braid events as described above and compute the FTBE using the *databraid* routine. Fig. 9b shows convergence of the scaled FTBE ($\Delta_L/\langle v_1 \rangle$ FTBE N_x) to the random braid entropy $\langle \lambda_\sigma \rangle$ with increasing number of braid events N_b and particles $N_p = N_x \times N_x$ for the 2D streamline model over 10 realisations of random braiding sequences. Hence for the scaled FTBE is related to the random braid entropy as

$$\lim_{N_b \rightarrow \infty} \lim_{N_p \rightarrow \infty} \frac{\Delta_L}{\langle v_1 \rangle} \text{FTBE } N_x = \langle \lambda_\sigma \rangle. \quad (15)$$

Budišić and Thiffeault [42] show that in limit of long times and large particle numbers the FTBE converges to the Lyapunov exponent $\hat{\lambda}_\infty$, hence the dimensionless Lyapunov exponent $\lambda_\infty \equiv \hat{\lambda}_\infty \ell / \langle v_1 \rangle$ converges to the scaled FTBE as

$$\frac{\ell}{\langle v_1 \rangle} \lim_{N_b \rightarrow \infty} \lim_{N_p \rightarrow \infty} \text{FTBE} = \lambda_\infty. \quad (16)$$

Squaring this expression yields

$$\lambda_\infty^2 = \frac{\ell^2}{\langle v_1 \rangle^2} \text{FTBE}^2 = \langle \lambda_\sigma \rangle^2 \frac{\ell^2}{\Delta_L^2} \frac{1}{N_p} \quad (17)$$

and substitution of (14) yields

$$\lambda_\infty^d = \langle \lambda_\sigma \rangle^d \frac{d D_T}{\langle v_1 \rangle \Delta_L} = \langle \lambda_\sigma \rangle^d \left(\frac{\ell}{\Delta_L} \right)^{d-1} \frac{d}{Pe_T}, \quad d = 1, 2. \quad (18)$$

Hence the 2D streamline model recovers equation (7) in the main body of the paper relating the Lyapunov exponent to the transverse dispersivity.

Extension of 2D Streamline Model to 2D Random Walk Model

To extend the 2D streamline model to a 2D random walk model, following [39] we generate N_p random streamlines in the domain $\Omega : (x_1, x_2, x_3) \in [0, \infty) \times [0, L] \times [0, L]$. As shown in Fig. 10a), the streamlines are all initiated at random locations within the $x_1 = 0$ plane in Ω and propagate longitudinally in the x_1 direction by steps of size Δ_L . During each step, the streamlines also make a step of magnitude Δ_T at a random direction (chosen such that the streamline remains confined within Ω) in the $x_2 - x_3$ plane.

The major differences between this random streamline model and the 1D and 2D streamline models discussed in the previous section is that (i) streamlines make a random walk rather than being confined to braiding within the streamline array, and (ii) all the streamlines undergo simultaneous braiding events similar to real flows, rather than the single braiding events encoded in the models derived from braid generators. We show below that these

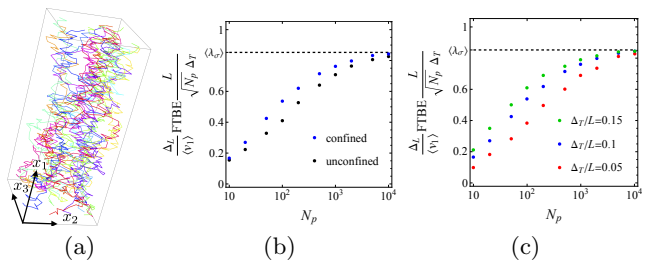


FIG. 10. (a) Schematic of 2D random walk streamline model. (b) Convergence of scaled FTBE (21) for the unconfined (black dots) and confined (blue dots) 2D random walk models to the random braid entropy $\langle \lambda_\sigma \rangle$ with the number N_p of streamlines and $N_{x_1} = 10^3$ random steps. (c) Convergence of scaled FTBE (21) to the random braid entropy $\langle \lambda_\sigma \rangle$ with the number N_p of streamlines for different values of Δ_T/L .

changes make no material differences to the transverse dispersion/fluid stretching relationship (9) derived in the main body of this paper.

Although confinement of streamlines to the domain Ω leads to zero transverse dispersivity, Fig. 8b shows that the braiding entropy of these random streamlines approaches that of unconfined streamlines as N_p becomes large. Hence the braiding entropy of this confined streamline model may be compared to the dispersivity of the unconfined streamline model. For the unconfined model, the transverse variances grow as

$$\sigma_{x_2}^2(t) = \sigma_{x_3}^2(t) = \sigma_0^2 + \frac{\Delta_T^2}{2} \frac{x_1}{\Delta_L} = \sigma_0^2 + \frac{\Delta_T^2}{2\Delta_L} \langle v_1 \rangle t, \quad (19)$$

as the number of random steps of size Δ_T is $x_1/\Delta_L = \langle v_1 \rangle t / \Delta_L$. As these variances both grow linearly as $2D_T t$, the relationship between transverse dispersivity D_T and the random walk parameters is then

$$D_T = \frac{\Delta_T^2}{4\Delta_L} \langle v_1 \rangle. \quad (20)$$

Fig. 10 shows that as the number of streamlines N_p and longitudinal increments $N_{x_1} = x_1/\Delta_L$ becomes large, the scaled FTBE converges to the random braid entropy as

$$\lim_{N_p \rightarrow \infty} \lim_{N_{x_1} \rightarrow \infty} \frac{\Delta_L}{\langle v_1 \rangle} \text{FTBE} \frac{1}{\sqrt{N_p}} \frac{L}{\Delta_T} = \langle \lambda_\sigma \rangle, \quad (21)$$

suggesting that braiding in the random streamline model is also governed by this universal constant. The different scaling of the FTBE for this model arises because all N_p streamlines braid at each longitudinal increment Δ_L , whereas for the 1D and 2D streamlines, only one braiding event occurs across all N_p streamlines respectively. As the streamlines in this random walk model all undergo independent random walks, then in the same manner as the 1D and 2D streamline models, the average spacing between nearest streamlines (given by $L/\sqrt{N_p}$)

is equivalent to the correlation length scale ℓ of the flow. Squaring (21) and substitution of (20) yields

$$\frac{\Delta_L^2}{\langle v_1 \rangle^2} \text{FTBE}^2 = \langle \lambda_\sigma \rangle^2 N_p \frac{\Delta_T^2}{L^2} = \langle \lambda_\sigma \rangle^2 \frac{N_p}{L^2} \frac{d^2 D_T \Delta_L}{\langle v_1 \rangle^2}, \quad (22)$$

Hence the relationship between Lyapunov exponent and transverse dispersivity is then

$$\lambda_\infty^2 = \langle \lambda_\sigma \rangle^2 \frac{d^2 D_T}{\langle v_1 \rangle \Delta_L} = \langle \lambda_\sigma \rangle^2 \frac{\ell}{\Delta_L} \frac{d^2}{Pe_T}. \quad (23)$$

Random Conductivity Fields

The random fields $f(\mathbf{x}) = \ln K(\mathbf{x})$ used for the hydraulic conductivity fields $k_0(\mathbf{x})$, $k_\delta(\mathbf{x})$ are given by the Fourier modes

$$f(\mathbf{x}) = \sum_{n=1}^2 \sum_{i,j,k}^{N_i} \frac{A_{n,ijk}}{\sqrt{i^2 + j^2 + k^2}} \cos(2\pi i(x_1 + \phi_{n,ijk}^1)) \cos(2\pi j(x_2 + \phi_{n,ijk}^2)) \cos(2\pi k(x_3 + \phi_{n,ijk}^3)), \quad (24)$$

where $N = 2$ is the number of Fourier modes and so the correlation length of these random fields is $\ell = 1/(2N)$. N_i is the number of realisations in each mode, and the coefficients $A_{n,ijk}$ and the phase angles $\phi_{n,ijk}$ are uniformly distributed random variables in $[0, 1]$ and the coefficient $\sum_{\ln k}^2$ is chosen such that the log-variance $\|f^2\|_{\mathcal{D}} = \sigma_{\ln k}^2 = 4$. We note that $N = 2$ is required to generate chaotic dynamics as symmetric conductivity fields (corresponding to $N = 1$) do not generate chaotic dynamics due to the symmetry of the resultant velocity field.

Darcy Flow Numerical Solvers and Streamline Tracking

To solve the divergence-free condition $\nabla \cdot \mathbf{v} = 0$ for the Darcy flow given by equation (9) in the main body of the paper over the triply-periodic domain \mathcal{D} , we decompose the potential field into mean and fluctuating components respectively as

$$\phi(\mathbf{x}) = \bar{\phi}(\mathbf{x}) + \tilde{\phi}(\mathbf{x}), \quad (25)$$

and set the mean potential as $\bar{\phi} = -x_1$. The resulting governing equation for the potential fluctuation $\tilde{\phi}(\mathbf{x})$ is then

$$\nabla \cdot (\mathbf{K} \cdot \nabla \tilde{\phi}(\mathbf{x})) = \nabla \cdot (\mathbf{K} \cdot \hat{\mathbf{e}}_1). \quad (26)$$

This equation is solved to precision 10^{-16} on a uniform structured 256^3 grid using a high resolution eighth-order compact finite difference scheme [45] via an iterative Krylov method. To generate high resolution results and preserve the Lagrangian kinematics of the flow,

we use a similar numerical approach to that used in [46]. Specifically, we perform a triply-periodic 5-th order spline interpolation of the primitive variables $\tilde{\phi}(\mathbf{x})$, $\mathbf{K}(\mathbf{x})$ from their grid values and reconstruct a smooth, continuous potential field $\phi(\mathbf{x})$ according to (25). The velocity field is then computed analytically from these fields as $\mathbf{v}(\mathbf{x}) = -\mathbf{K}(\mathbf{x}) \cdot \nabla \phi(\mathbf{x})$, ensuring that the velocity field is triply-periodic and C_4 continuous and the velocity gradient is accurately resolved. For the 256^3 mesh the local relative divergence error

$$d(\mathbf{x}) = \frac{|\nabla \cdot \mathbf{v}(\mathbf{x})|}{\|\nabla \mathbf{v}(\mathbf{x})\|}, \quad (27)$$

of the interpolated velocity field $\mathbf{v}(\mathbf{x})$ is order 10^{-4} and the velocity gradient is accurate to order 10^{-3} . Streamline tracking is then computed by solving the advection equation from the initial Lagrangian coordinate \mathbf{X} as

$$\frac{d\mathbf{x}}{dt} = \mathbf{v}(\mathbf{x}(t; \mathbf{X})), \quad \mathbf{x}(0; \mathbf{X}) = \mathbf{X}, \quad (28)$$

via a 5-th order Cash-Karp Runge-Kutta scheme to precision 10^{-14} . The periodic boundaries allow advection of fluid streamlines over many multiples of the solution domain \mathcal{D} , facilitating study of the Lagrangian kinematics over arbitrary distances. Although the corresponding velocity field is periodic in space, when the flow is chaotic the streamlines are aperiodic and eventually sample all of the conductivity field in an ergodic manner.

While accurate, this streamline tracking method (along with all numerical schemes which do not explicitly enforce kinematic constraints) has been shown [37] to introduce spurious transverse dispersion for the helicity-free flow $h = 0$ due to numerical streamlines not following their analytic counterparts. To circumvent this problem for the helicity-free case $\delta = 0$, we instead solve the invariant streamfunctions $\psi_1(\mathbf{x})$, $\psi_2(\mathbf{x})$ for the velocity field $\mathbf{v}(\mathbf{x}) = \nabla \psi_1(\mathbf{x}) \times \nabla \psi_2(\mathbf{x})$ via the following governing equations [47] to precision 10^{-16} using the same finite-difference method as described above:

$$\nabla^2 \psi_1(\mathbf{x}) - \nabla f(\mathbf{x}) \cdot \nabla \psi_1(\mathbf{x}) = S_1(\psi_1, \psi_2), \quad (29)$$

$$\nabla^2 \psi_2(\mathbf{x}) - \nabla f(\mathbf{x}) \cdot \nabla \psi_2(\mathbf{x}) = S_2(\psi_1, \psi_2), \quad (30)$$

where $f = \ln k$ and

$$S_1 = \frac{(\mathbf{B} \times \psi_2) \cdot (\nabla \psi_1 \times \nabla \psi_2)}{|\nabla \psi_1 \times \nabla \psi_2|} \quad S_2 = \frac{(\mathbf{B} \times \psi_1) \cdot (\nabla \psi_1 \times \nabla \psi_2)}{|\nabla \psi_1 \times \nabla \psi_2|}, \quad (31)$$

and

$$\mathbf{B} \equiv (\nabla \psi_1 \cdot \nabla) \nabla \psi_2 - (\nabla \psi_2 \cdot \nabla) \nabla \psi_1. \quad (32)$$

Similar to the Darcy equation, continuous streamfunctions $\psi_1(\mathbf{x})$, $\psi_2(\mathbf{x})$ are reconstructed from grid data

using triply-periodic splines and the velocity field is computed analytically from these streamfunctions. As shown in [47], this method yields the same velocity field (to within numerical error) as that given by direct solution of the Darcy equation.

Each family of streamfunctions ψ_i is comprised of a *foliation* of non-intersecting streamsurfaces $\psi_i = \text{const.}$ that span the flow domain and constrain the Lagrangian kinematics of the flow. This flow structure is non-chaotic as the advection equation (28) simplifies to

$$\frac{ds}{dt} = v(s; \psi_1(\mathbf{X}), \psi_2(\mathbf{X})), \quad s(t=0; \mathbf{X}) = 0, \quad (33)$$

where s is the distance travelled along a streamline of a tracer particle with initial position \mathbf{X} . The velocity magnitude $v(s; \psi_1(\mathbf{X}), \psi_2(\mathbf{X}))$ at the intersection of the streamsurfaces $\psi_1(\mathbf{x}) = \psi_1(\mathbf{X})$, $\psi_2(\mathbf{x}) = \psi_2(\mathbf{X})$ only varies with s . Equation (33) is *integrable* in that ψ_1, ψ_2 represent two invariants of the flow in the 3D domain, resulting in only one degree of freedom (distance) for streamlines of the flow to explore. Lester *et al.* [37] subsequently proved that the confinement of streamlines to streamsurfaces ψ_1, ψ_2 prohibits transverse hydrodynamic dispersion in the asymptotic limit if the isotropic conductivity field $k(\mathbf{x})$ is smooth, regardless of the heterogeneity or conductivity structure of the medium at the Darcy scale. For helicity-free flow, we perform streamline tracking via numerical integration of (33) to precision 10^{-8} . This approach ensures numerical streamlines follow their analytic counterparts and so enforces zero transverse dispersion and prevents the non-trivial braiding of streamlines that lead to chaotic advection.

Calculation of Transverse Dispersivity

For both the steady 3D Darcy flow and the unsteady 2D time-periodic random sine flow (TPRSF), the transverse dispersivity is determined by tracking $N_p = 10^3$ streamlines or pathlines respectively over 10^3 traverses of the periodic domain \mathcal{D} seeded from random locations within \mathcal{D} or 10^3 flow periods T . From the 3D streamlines and the 2D pathlines, the transverse variances are computed as

$$\sigma_{x_j}^2(t) = \frac{1}{N_p} \sum_{i=1}^{N_p} (x_{j,i}(t) - \langle x_j \rangle(t))^2, \quad \langle x_j \rangle(t) = \frac{1}{N_p} \sum_{i=1}^{N_p} x_{j,i}(t), \quad (34)$$

where $j = 1, 2$ for the TPRSf and $j = 2, 3$ for the 3D Darcy flow. The transverse dispersivities are then related to the asymptotic variance growth as

$$D_{jj} = \frac{1}{2} \lim_{t \rightarrow \infty} \frac{d\sigma_{x_j}^2}{dt}, \quad (35)$$

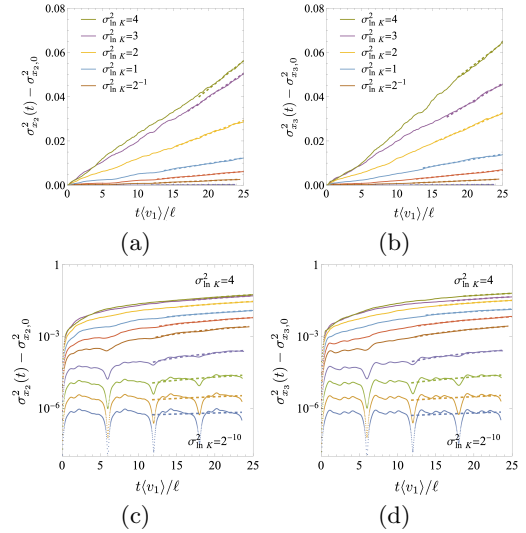


FIG. 11. Evolution of transverse scalar variances $\sigma_{x_2}^2(t)$ (left), $\sigma_{x_3}^2(t)$ (right) with dimensionless travel time $t\langle v \rangle/\ell$ in linear (top) and logarithmic (bottom) scales for steady heterogeneous anisotropic 3D Darcy flow for various values of log-conductivity variance $\sigma_{\ln K}^2$. Fitted linear trend (dashed lines) at late times is used to estimate transverse dispersivity.

To estimate this asymptotic growth for both the TPRSf and the steady 3D Darcy flow we fit a linear function to the asymptotic variance data over two periods of the flow as shown in Fig. 11 for the 3D Darcy flow. Note that the variance data in Fig. 11 has been truncated to 20 correlation lengths for illustrative purposes. For both the TPRSf and the steady 3D Darcy flow the transverse dispersivity D_T is then computed as the average of the D_{jj} dispersivities.

As shown in Fig. 11 for the anisotropic Darcy flow with variable heterogeneity, for small conductivity variance $\sigma_{\ln K}^2 \ll 1$, the transverse variances exhibit slow growth and periodic oscillations as the streamlines of the flow are nearly periodic. With increasing heterogeneity $\sigma_{\ln K}^2$, these orbits lose periodicity and ergodically explore the flow domain, resulting in stronger growth of the transverse variances.

Computation of Lyapunov Exponents

For the TPRSf, the Lyapunov exponent of these flows is computed by directly integrating the deformation gradient tensor $\mathbf{F}(\mathbf{X}, t)$ along pathlines with Lagrangian coordinate \mathbf{X} as

$$\frac{d\mathbf{F}(\mathbf{X}, t)}{dt} = \boldsymbol{\epsilon}(\mathbf{X}, t) \cdot \mathbf{F}(\mathbf{X}, t), \quad \mathbf{F}(\mathbf{X}, 0) = \mathbf{1}, \quad (36)$$

where $\boldsymbol{\epsilon}(\mathbf{X}, t) \equiv \nabla \mathbf{v}(\mathbf{x}, t)^\top|_{\mathbf{x}=\mathbf{x}_0(\mathbf{X}, t)}$ and $\mathbf{x}_0(\mathbf{X}, t)$ is the position of a streamline initially at position \mathbf{X} at time $t =$

0. The simplicity of the TPRSf means that the evolution equation (36) can be solved analytically over each flow period T , and the finite time Lyapunov exponent for each streamline computed as

$$\hat{\lambda}(t, \mathbf{X}) = \frac{1}{t} \ln \nu(t, \mathbf{X}), \quad (37)$$

where $\nu(t, \mathbf{X})$ is the leading eigenvalue of the Cauchy-Green tensor $\mathbf{F}(\mathbf{X}, t)^\top \cdot \mathbf{F}(\mathbf{X}, t)$. The infinite-time Lyapunov exponent is then computed via the ensemble average

$$\hat{\lambda}_\infty = \lim_{t \rightarrow \infty} \langle \hat{\lambda}(t, \mathbf{X}) \rangle. \quad (38)$$

The Lyapunov exponent for the steady 3D Darcy flows is computed via the moving and rotating *Protean* coordinate frame as is detailed in [48] and briefly summarised as follows. The Protean coordinate frame \mathbf{x}' is related to the Eulerian frame \mathbf{x} as $\mathbf{x}'(t) = \mathbf{Q}(t) \cdot (\mathbf{x} - \mathbf{x}_0(t))$, where $\mathbf{x}_0(t)$ is the position of a fluid tracer particle at time t with initial position \mathbf{X} , and $\mathbf{Q}(t)$ is a time-dependent orthogonal rotation matrix. The Protean velocity gradient tensor $\epsilon'(\mathbf{x}', t)$ is related to the Lagrangian velocity gradient tensor $\epsilon(\mathbf{X}, t)$ as

$$\epsilon'(\mathbf{X}', t) = \mathbf{Q}^\top(t) \cdot \epsilon(\mathbf{X}, t) \cdot \mathbf{Q}(t) + \dot{\mathbf{Q}}^\top(t) \cdot \mathbf{Q}(t), \quad (39)$$

where $\epsilon(\mathbf{X}, t) \equiv \nabla \mathbf{v}(\mathbf{x})^\top|_{\mathbf{x}=\mathbf{x}_0(\mathbf{X}, t)}$. The rotational matrix $\mathbf{Q}(t)$ aligns the x'_1 coordinate with the local velocity direction \mathbf{v}/v , and for steady flow the Protean coordinate system is a streamline coordinate system. The rotation $\mathbf{Q}(t)$ is comprised of two subrotations as $\mathbf{Q}(t) = \mathbf{Q}_2(t) \cdot \mathbf{Q}_1(t)$, where the first rotation $\mathbf{Q}_1(t)$ aligns x'_1 with \mathbf{v}/v and so renders the ϵ'_{21} and ϵ'_{31} elements of the Protean velocity gradient tensor $\epsilon'(t)$ to be zero [48]. The second rotation $\mathbf{Q}_2(t)$ about the axis \mathbf{x}' in the streamwise direction is chosen such the remaining lower triangular element ϵ'_{23} is also zero [48], rendering the Protean velocity gradient tensor upper triangular:

$$\epsilon' = \begin{pmatrix} \epsilon'_{11} & \epsilon'_{12} & \epsilon'_{13} \\ 0 & \epsilon'_{22} & \epsilon'_{23} \\ 0 & 0 & \epsilon'_{33} \end{pmatrix}. \quad (40)$$

This greatly simplifies solution of the deformation gradient tensor $\mathbf{F}'(\mathbf{X}', t)$ as

$$\frac{d\mathbf{F}'(\mathbf{X}', t)}{dt} = \epsilon'(\mathbf{X}', t) \cdot \mathbf{F}'(\mathbf{X}', t), \quad \mathbf{F}'(\mathbf{X}', 0) = \mathbf{1}, \quad (41)$$

which is related to its Lagrangian counterpart as

$$\mathbf{F}'(\mathbf{X}', t) = \mathbf{Q}^\top(t) \cdot \mathbf{F}(\mathbf{X}, t) \cdot \mathbf{Q}(0), \quad (42)$$

and $\mathbf{F}'(\mathbf{X}', t)$ is also upper triangular. The major advantage of the Protean frame is that the diagonal components ϵ'_{ii} and F'_{ii} represent the principal stretches of material elements, whereas the non-zero off-diagonal components ϵ'_{ij} , $j > i$, represent shear deformations. This means that in the Protean frame, the hyperbolic stretches that directly govern the Lyapunov exponents of the flow are not conflated with other deformations such as shears and rotations, and so may be directly measured from the diagonal components ϵ'_{ii} . Indeed, the diagonal elements of $\mathbf{F}'(\mathbf{X}', t)$ grow exponentially with the diagonal elements of $\epsilon'(t)$ as

$$F'_{ii}(t) = \exp\left(\int_0^t dt' \epsilon'_{ii}(t')\right), \quad i = 1 : 3. \quad (43)$$

From (43), fluid stretching in the streamwise direction simply fluctuates with the local velocity as $F'_{11}(t) = v(t)/v(0)$ but do not grow in random stationary flows as $\langle F'_{11} \rangle \sim 1$. Conversely, the transverse stretches F'_{22} and F'_{33} respectively grow and decay exponentially according to the Lyapunov exponent as $\langle F'_{22} \rangle = 1/\langle F'_{33} \rangle \sim \exp(\lambda_\infty t)$.

Due to linearity of the Darcy equation, we non-dimensionalise the velocity gradient in terms of the mean velocity and correlation length as

$$\tilde{\epsilon}'(\mathbf{X}', t) \equiv \frac{\ell}{\langle v \rangle} \epsilon'(\mathbf{X}', t), \quad (44)$$

Using this non-dimensionalisation the dimensionless Lyapunov exponent λ_∞ can be quantified directly in terms of the ensemble averages $\langle \tilde{\epsilon}'_{ii} \rangle$, $i = 2, 3$ as

$$\lambda_\infty = \langle \tilde{\epsilon}'_{22} \rangle = -\langle \tilde{\epsilon}'_{33} \rangle, \quad (45)$$

with $\langle \tilde{\epsilon}'_{11}(t) \rangle = 0$ and the divergence-free condition manifests as $\sum_i \tilde{\epsilon}'_{ii} = 0$. Hence to leading order chaotic advection in steady 3D flow is characterised by the Lyapunov exponent λ_∞ .

Previous studies [49, 50] have established that for steady flows in random media at both the pore- and Darcy scales, the velocity magnitude v decorrelates along streamlines in space rather than time (whereas the velocity magnitude exhibits strong intermittency in time), such that the velocity follows a spatial Markovian process with respect to the correlation length ℓ . Lester *et al.* [48] showed that the velocity gradient ϵ also follows a spatial Markovian process and also decorrelates with respect to the correlation length ℓ . The Protean velocity gradient ϵ' is computed along the 10^3 streamlines of the flow for a distance of $10^3 \ell$ and is sampled at fixed spatial increment ℓ , yielding $n = 10^6$ independent observations. Although the distributions of ϵ'_{ii} for $i = 1 : 3$ are broad, with standard deviation $\sigma_{\epsilon'_{ii}}^2 \sim 1$, the large number n of independent observations reduces the standard error of λ_∞ in (45) to $\sigma_{\epsilon'_{ii}}^2 / \sqrt{n} \sim 10^{-3}$.